nature communications

Article

https://doi.org/10.1038/s41467-026-70693-9

Sustained hydrogen peroxide production via MXene-functionalized supramolecular docking

Received: 8 July 2025

Accepted: 3 March 2026

Published online: 15 March 2026

Check for updates

Jiaxun Sun[1,2,5], Yuanming Zhang[1,5], Wanheng Lu[1], Wei Li Ong[1], Xinglong Pan[1], Wentao Song[3], Zhonghua Li[4], Zhaosheng Li[4] & Ghim Wei Ho[1,2]

Direct photosynthesis of hydrogen peroxide (H_2O_2) from air and water using metal/covalent-organic frameworks offers a sustainable alternative to the conventional energy-intensive anthraquinone process. However, current systems suffer from short operational lifetimes typically 10–100 h due to mismatches between O_2 capture efficiency and multielectron redox kinetics. Here, we report a supramolecular platform that integrates O_2 capture, H_2O_2 synthesis, and in situ utilization, enabling continuous H_2O_2 production for over 1000 h without sacrificial agents. Mesoporous bromine-substituted COFs are hydrogen-bonded to photothermal MXene, providing organized O_2 docking sites and columnar charge transport via σ-σ interactions and π-π stacking. Through a dual-pathway mechanism, the architecture achieves a competitive H_2O_2 production rate of 2878 μmol g^{-1} h^{-1}, alongside complete pollutant removal and durable operation across diverse water sources and outdoor conditions. This work demonstrates a supramolecular design featuring programmable O_2 docking, directional charge transport, and localized H_2O_2 utilization toward decentralized chemical manufacturing.

Hydrogen peroxide (H_2O_2) has been extensively used as a clean oxidant in bleaching, disinfection, environmental remediation, and organic synthesis[1]. More recently, it has emerged as a promising zero-emission liquid fuel, capable of converting chemical energy into electricity with minimal pollution and high cost-efficiency[2]. Today's industrial production of H_2O_2 is dominated by the conventional anthraquinone oxidation (AO) process, which requires multistep hydrogenation–oxidation cycles at elevated temperatures to activate reagents[3] (Supplementary Fig. 1a). This not only incurs substantial energy penalties but also generates large volumes of wastewater, exhaust gases, and solid waste, undermining its environmental credentials and raising downstream treatment costs. Therefore, photocatalytic H_2O_2 synthesis with green and mild reaction conditions has been considered as an alternative approach. Although inorganic catalysts (TiO_2, CdS, and g-C_3N_4) have been widely explored for electro/photo synthesis[4,5], their periodic lattice lacks robust docking sites and efficient transport channels, hindering the material's ability to capture O_2 from open air and rapidly transfer H_2O molecules, thereby limiting its conversion efficiency (Supplementary Fig. 1b). Covalent organic frameworks (COFs) with donor-acceptor structures offer high porosity, crystallinity, and tunable band structures, and have shown promise for photocatalytic H_2O_2 production. Despite conventional strategies including band structure tuning and suppression of photogenerated carrier recombination, their photocatalytic activities remain hampered by an inherently weak photoresponse. In particular, harnessing near-infrared light (NIR, >760 nm), which accounts for ~53 % of solar

[1]Department of Electrical and Computer Engineering, National University of Singapore, Singapore, Singapore. [2]Department of Materials Science and Engineering, National University of Singapore, Singapore, Singapore. [3]Department of Chemical and Biomolecular Engineering, National University of Singapore, Singapore, Singapore. [4]Collaborative Innovation Center of Advanced Microstructures, National Laboratory of Solid State Microstructures, College of Engineering and Applied Sciences, Nanjing University, Nanjing, China. [5]These authors contributed equally: Jiaxun Sun, Yuanming Zhang.
e-mail: elehgw@nus.edu.sg

irradiance, could drastically enhance catalytic performance[6], yet few COFs successfully combine NIR photo-absorbers with efficient, well-defined charge transfer pathways.

To mimic the multi-unit architecture of respiratory enzymes in living organisms optimized for O_2 and H_2O molecules utilization and maintain the same dynamic response as the conventional metal-organic frameworks (MOFs), we proposed a versatile supramolecular system that can be universally employed to integrate various frameworks and functional building units. In specific, we incorporate metallic amine-functionalized MXene ($Ti_3C_2T_x$-NH_2) photothermal units into rigid COF backbones to construct an integrated supramolecular $(COF)_x$-NH_2-M system (where x refers to the mass ratio between COF and MXene, supported by the elemental analysis in Supplementary Tables 1 and 2) for the capture–synthesis–utilization of H_2O_2 (Fig. 1a), exhibiting a MOFs-like light harvesting characteristics enhanced by the presence of metallic units. Hydrogen-bonded interactions on highly electronegative N atoms links conjugated layers via π-π stacking interactions, while σ-σ stacking interactions[7] connect multilayered nanosheets, creating densely organized O_2-docking sites and rapid, directional charge pathways (Fig. 1b). To guide supramolecular assembly for controlled crystallinity, surface area and carrier mobility[8], we surmise that TAPB (1,3,5-tris(4-aminophenyl)benzene) monomer, among the common ligands[9], maximizes hydrogen-bonded interactions by providing the highest density of N sites, thereby promoting intermolecular charge transfer (Fig. 1c). Compared to triazine, the decentralized spatial distribution of N atoms in TAPB further promotes charge separation throughout catalytic reactions.

The highly tunable pore structures in COFs confine guest molecules within their channels through multiple van der Waals interactions, theoretically supporting efficient molecular recognition for selective gas capture. However, O_2 and N_2 molecules in air have remarkably similar kinetic diameters (3.46 and 3.64 Å, respectively)[10],

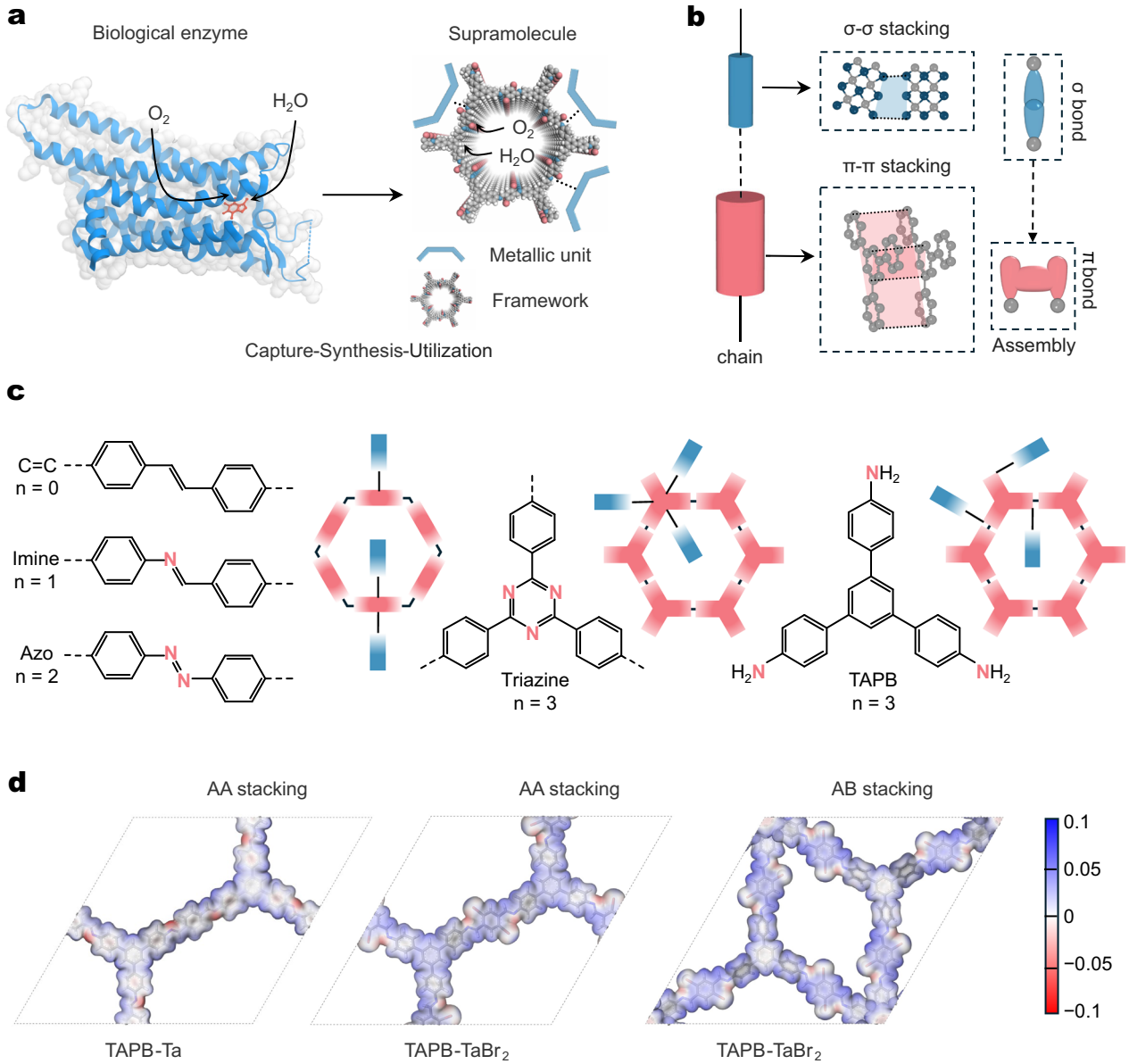

Fig. 1 | Molecular design of metallic unit-functionalized hydrogen-bonded supramolecular assemblies with docking sites. a Schematic of integrated supramolecular design featuring enzyme-like docking sites for various frameworks and functional units. **b** σ-π assembly contributed by the connection of σ-σ and π-π stacking interactions (dash line on the chain represents hydrogen bonds). **c** Molecular design of N-rich ligands with steric effects (blue, metallic MXene units; red, COF ligands). **d** Electrostatic potential distribution maps of TAPB-Ta COF in AA stacking, TaPB-$TaBr_2$ COF in AA stacking, and TAPB-$TaBr_2$ COF in AB stacking, the unit of scale bar is Hartree/e.

limiting the specificity of O_2 capture. To elaborate, O_2 is a paramagnetic molecule possessing two unpaired electrons in its π* orbital, which allows it to engage in coordination or charge-transfer complexes with hosts featuring vacant orbitals or donor sites. In contrast, the chemically inert, diamagnetic N_2 molecule with its stable triple bond exhibits minimal propensity for similar electron interactions and docking affinity toward supramolecular framework. In addition to the intrinsically higher electron affinity of O_2, the presence of electron-deficient centers (such as aromatic nitrogen heterocycles[11] and conjugated quinones[12]) in aromatic molecules have been shown to preferentially adsorb O_2. Besides, water molecules serves as proton donors for H_2O_2 production renders their interaction with the COF structure essential for tailoring the overall reactivity and durability[13]. To address these challenges, we herein introduce a docking strategy based on the π-conjugated structure of our supramolecular materials and the electron configuration of O_2. Although recent advancements have underscored the potential of molecular docking in drug design for predicting ligand-receptor interactions[14–16], a comprehensive understanding of docking mechanisms in catalytic reactions remains to be fully established to enable their efficient application.

In this work, we incorporate bromine, a more electronegative substitute for carbon to induce the delocalization of π-electrons, thereby lowering the electron density of benzene rings. The AA-stacked TAPB-$TaBr_2$ COF (where $TaBr_2$ is 2,5-dibromoterephthalaldehyde) exhibits the largest electrostatic potential variation, optimizing distinct molecular docking sites for O_2 (Fig. 1d and Supplementary Fig. 2). Our theoretical calculations confirm that O_2 adsorption at theses aromatic docking sites is energetically favored within the supramolecular framework. Notably, variations in binding affinity across different sites of supramolecular assemblies are closely related to the adsorption-desorption dynamics underpinning target-molecule capture and release. The intrinsic mesoporous architecture of COF frameworks exposes abundant, spatially defined sites for O_2 and H_2O adsorption, maximizing opportunities for molecular reactant docking. Thereby, we establish a well-defined supramolecular catalyst, enabling two key advances (i) optimized charge transfer through σ-π hydrogen-bonded connection and (ii) efficient catalytic turnover through strategic reactant-catalyst docking. Simultaneously, $(COF)_x$-NH_2-M exhibits a broadened light absorption into the NIR region and harnesses photothermal heating of hot electrons to drive the photosynthesis of H_2O_2 at elevated local temperatures.

Results

Structure of COF and supramolecular photocatalysts

In the $(COF)_x$-NH_2-M supramolecular system, TAPB-$TaBr_2$ COF is introduced with Br substituents derived from TAPB-Ta COF (where Ta is terephthalaldehyde), a selected prototype for H_2O_2 photocatalysis[17]. Solvothermal condensation of TAPB with $TaBr_2$ yields an imine-linked COF designed to feature (i) mesopores for efficient mass transfer without requiring additional activation, (ii) electron-donating TAPB "knots" to drive four-electron water oxidation reaction (WOR), and (iii) electron-accepting $TaBr_2$ linkers for two-electron oxygen reduction (ORR)[13]. The rigid Br substituents in TAPB-$TaBr_2$ COF induce a distortion on Ta backbones (Supplementary Fig. 3), resulting in stronger interplanar interactions, enhancing thermal stability and crystallinity[18]. To stabilize the MXene and improve its supramolecular interactions, $Ti_3C_2T_x$ nanosheets are functionalized with 3-aminopropyltriethoxysilane (APTES), yielding NH_2-terminated surfaces that circumvent phase transformation[19] under photocatalytic process and boost hydrogen-bonded bridging with TAPB-$TaBr_2$ COF (Supplementary Fig. 4a). To elucidate the local intermolecular interaction on imine linkages, we employed the Independent Gradient Model based on Hirshfeld partitioning (IGMH) to analyze weak interaction (Fig. 2a). The density functional theory (DFT) optimized cluster model clearly reveals the formation of N–H···N hydrogen bonds (2.20 Å). The green IGMH isosurface with faint blue center localized at the hydrogen bonding sites indicates the coexistence of van der Waals interaction and weak hydrogen bonding interaction[20]. The distribution of most data points between −0.02 and 0.01, together with the relatively larger δg values near 0.02 in the scatter plot, further supports our proposal. N 1*s* X-ray photoelectron spectroscopy (XPS) results verify the bridging on N atoms, with N–H peak (401.6 eV) significantly enhanced by amino hydrogen bonding, while the N = C peak (399.5 eV)[21] remains unchanged (Fig. 2b). Moreover, the Fourier transform infrared (FTIR) spectra of $Ti_3C_2T_x$-NH_2 composite under $TaBr_2$ monomers presence at varied duration exhibit no detectable enhancement on C = N absorption, confirming the absence of covalent bond formation between $Ti_3C_2T_x$-NH_2 and TAPB-$TaBr_2$ COF (Supplementary Fig. 5).

The highly ordered π-π stacked COF backbone is evident from its theoretically consistent crystal configuration and mesoporous architecture. The crystal structure of TAPB-$TaBr_2$ COF in AA stacking (Supplementary Fig. 4b) was optimized by DFT (Supplementary Tables 3–5) and reconstructed by Pawley refinement with lattice parameters of a = b = 3.62 nm, c = 0.419 nm, $\alpha = \beta = 90°$, and $\gamma = 120°$. Powder X-ray diffraction pattern (PXRD) patterns (Fig. 2c) confirm the AA-stacked hexagonal framework, while other symmetries and stacking modes fail to reproduce the observed intralayer atom distributions and peak positions (Supplementary Figs. 3 and 6). Solid-state ^{13}C cross-polarization magic angle spinning nuclear magnetic resonance (CP/MAS NMR) spectroscopy further verifies the distinct carbon environments along the imine linkages (Supplementary Fig. 7). To assess COF quality, Raman spectroscopy shows the absence of $TaBr_2$ aldehyde C=O stretching vibration around 1690 cm^{-1}, alongside an intense phenyl C=C band at ~1570 cm^{-1}, and a C=N band at 1616 cm^{-1} (Supplementary Fig. 8), indicating monomer depletion and imine bond formation. Similarly, characteristic peaks for imine COF with highly conjugated aromatic rings are observed at 1615 cm^{-1} and 1594 cm^{-1} in FTIR spectrum of TAPB-$TaBr_2$ COF (Supplementary Fig. 9). Nitrogen sorption measurements at 77 K determine the high Brunauer-Emmett-Teller (BET) surface areas of 1289.56 $m^2\ g^{-1}$ for TAPB-$TaBr_2$ COF and 1125.70 $m^2\ g^{-1}$ for $(COF)_{2.5}$-NH_2-M. Both reveal type VI isotherms accompanied by H2-type hysteresis, confirming the extensive presence of columnar pores and interparticle voids (Supplementary Fig. 10). Barrett-Joyner-Halenda (BJH) analysis shows a dominant micropore width of 3.79 nm (Supplementary Fig. 11), which is consistent with the pore size predicted from the crystal structure (37.274 Å from Supplementary Fig. 3a). The resulting structural stability and mesoporosity expose abundant binding sites, enabling efficient docking of O_2 molecules.

In addition, detailed analysis of the chemical states associated with σ-σ units was performed for both the MXene and the supramolecular assembly. APTES grafting on single-layered $Ti_3C_2T_x$ MXene was verified by solution-state ^1H NMR (Supplementary Fig. 12) and Raman spectroscopy (Supplementary Fig. 8b), which show signals attributed to silane hydrolysis and amino (–NH_2) groups. XPS survey scans of $Ti_3C_2T_x$-NH_2, TAPB-$TaBr_2$ COF, and the assembled $(COF)_x$-NH_2-M supramolecular catalysts reveal additional N 1*s* and Si 2*p* peaks (Supplementary Figs 13–17). The N–H peak in the N 1*s* XPS spectrum (Supplementary Fig. 15f) and the Si–O/Si–C peak (101.9 eV) in the Si 2*p* XPS spectrum (Supplementary Fig. 15g) suggest the coexistence of silane chains and amino groups. In addition, the increased intensity of the C–O peak around 286.2 eV in the C 1*s* XPS spectrum (Supplementary Fig. 15b) and the Ti(VI)–O doublet in the Ti 2*p* XPS spectrum (Supplementary Fig. 15c) confirms the formation of an oxygen bridge between MXene surface and the silane chain via hydrolysis reaction. The C 1*s* XPS spectrum of $(COF)_{2.5}$-NH_2-M exhibits characteristic peaks composed of C–Ti (281.8 eV), C=C/C–C (284.6 eV) and C=N (285.4 eV), which were respectively assigned to metallic MXene units, aromatic rings, and imine linkages (Supplementary Figs. 16 and 17). Detection of the Ti 2*p* XPS spectrum in $(COF)_{2.5}$-NH_2-M sample (Supplementary

https://doi.org/10.1038/s41467-026-70693-9

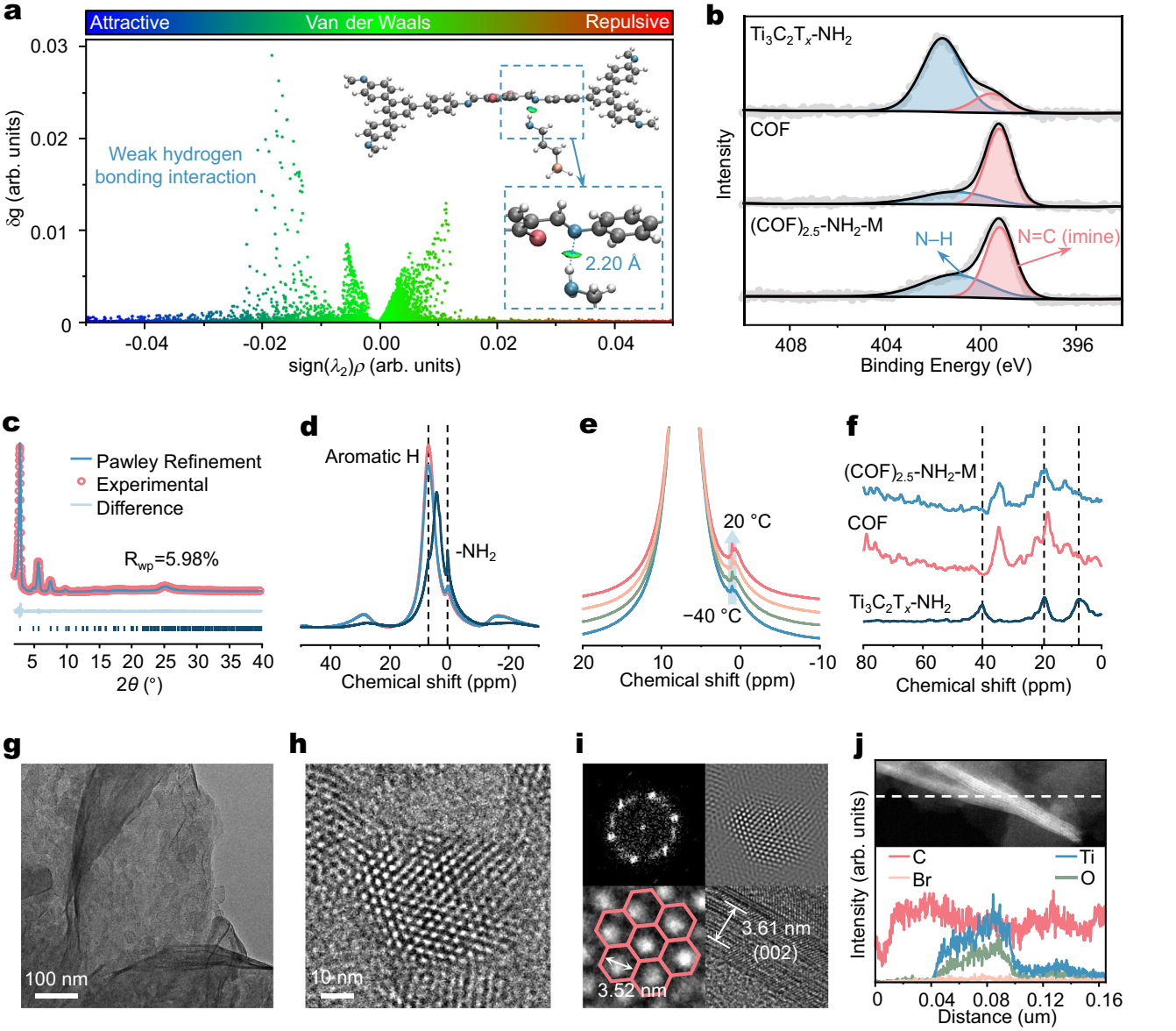

Fig. 2 | Structural characteristics of TAPB-TaBr$_2$ COF and supramolecular (COF)$_x$-NH$_2$-M. a IGMH analysis on molecular cluster models of TAPB-TaBr$_2$ COF and $Ti_3C_2T_x$-NH$_2$ (gray for C; blue for N; red for Br; light orange for Si; blue dash box for zoom-in details of hydrogen bonds). **b** N 1*s* XPS spectra of $Ti_3C_2T_x$-NH$_2$, TAPB-TaBr$_2$ COF, and (COF)$_{2.5}$-NH$_2$-M. **c** Experimental PXRD pattern of TAPB-TaBr$_2$ COF with Pawley refinement fit (Bragg positions are indicated with blue ticks). **d**, **f** Solid-state NMR spectra of $Ti_3C_2T_x$-NH$_2$ (dark blue), TAPB-TaBr$_2$ COF (red), and (COF)$_{2.5}$-NH$_2$-M (blue) **(d)** ^{1}H and **(f)** ^{13}C. **e** Variable-temperature ^{1}H solid-state NMR spectra of (COF)$_{2.5}$-NH$_2$-M (from −40 °C to 20 °C with an increment of 20 °C). **g**, **h** HR-TEM image of (COF)$_{2.5}$-NH$_2$-M in different magnification. **i** Fourier transform of the COF domains, showing lattice fringes of the COF networks and MXene multilayers. **j** EDS line scan (along the dash line) profiles of selected elements across the (COF)$_{2.5}$-NH$_2$-M.

Fig. 17e), along with the increased intensity of the $Ti_3C_2T_x$-NH$_2$ (002) peak at $2\theta = 4.3°$ in the PXRD patterns of (COF)$_x$-NH$_2$-M further confirms the retention of both MXene and COF phases (Supplementary Fig. 18).

Specifically, the reliability of the supramolecular assembly was confirmed through the validation of hydrogen-bonded bridges and morphological characterization. FTIR spectroscopy and NMR analysis distinguish hydrogen bond formation within the supramolecular assembly from covalent linking. As shown in Supplementary Fig. 9, the splitting and shifting[22] of the C=N/C–N stretching peaks around 1693/1393 cm^{-1} in the FTIR spectra reveal the redistribution of electron density around the N center induced by N–H···N hydrogen bonding at the imine linkage in (COF)$_{2.5}$-NH$_2$-M. Similarly, the signal around 0.6 ppm (–NH$_2$) in ^{1}H NMR of (COF)$_{2.5}$-NH$_2$-M becomes broader in TAPB-TaBr$_2$ COF and sharper in $Ti_3C_2T_x$-NH$_2$, indicating the extensive formation of N–H···N hydrogen bonding at the interface to offset the electron shielding effect by conductive matrix of MXene (Fig. 2d). This assertion is further evidenced by the variable-temperature NMR results under ultrafast MAS conditions, presenting an increasing intensity of –NH$_2$ peaks due to the weakening hydrogen bonds with temperature rising[23] (Fig. 2e and Supplementary Fig. 19). Furthermore, the distinct signal around 40 ppm in ^{13}C NMR spectrum of $Ti_3C_2T_x$-NH$_2$ is slightly shifted in (COF)$_{2.5}$-NH$_2$-M (Fig. 2f), reflecting the effect of hydrogen bonding on the carbon atoms adjacent to the amino terminals. Scanning electron microscopy (SEM) images show that the TAPB-TaBr$_2$ COF forms granules ~2 μm in diameter (Supplementary Fig. 20a, b). With the incorporation of $Ti_3C_2T_x$-NH$_2$, COF particles uniformly assembled and stacked onto the metallic MXene nanosheets via supramolecular

https://doi.org/10.1038/s41467-026-70693-9

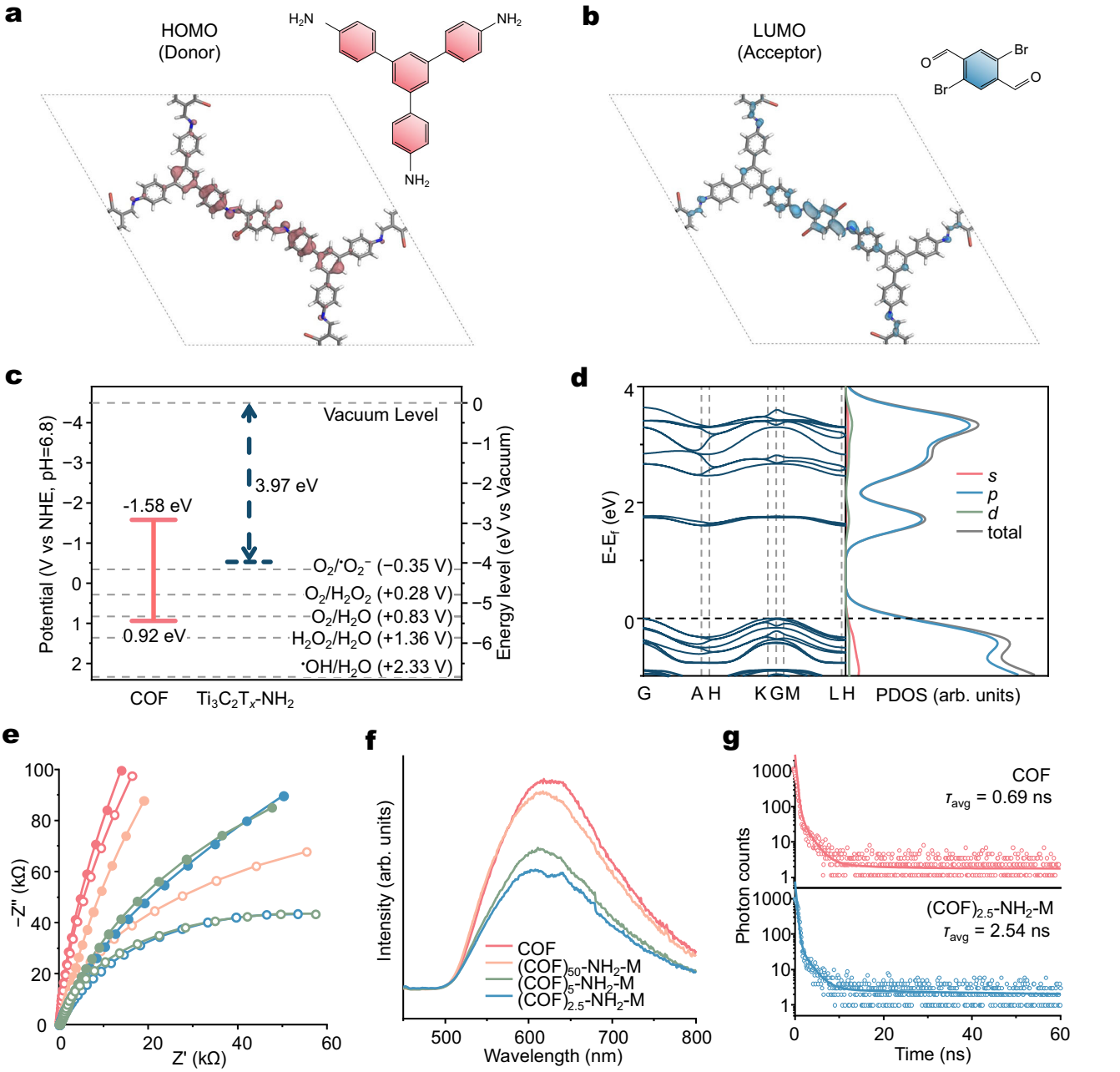

Fig. 3 | Band structure and photogenerated carrier dynamics of supramolecular (COF)$_x$-NH$_2$-M. a HOMO distribution of TAPB-TaBr$_2$ COF. **b** LUMO distribution of TAPB-TaBr$_2$ COF. **c** Experimentally derived energy band alignments of TAPB-TaBr$_2$ COF and $Ti_3C_2T_x$-NH$_2$. **d** Simulated band structure and PDOS of TAPB-TaBr$_2$ COF. **e** Electrochemical impedance spectra of (COF)$_x$-NH$_2$-M (solid circle for dark condition; hollow circle for 100 mW cm^{-2} light irradiation; orange for $x = 50$; green for $x = 5$; blue for $x = 2.5$). **f** Steady-state photoluminescence of (COF)$_x$-NH$_2$-M. **g** Transient fluorescence decay lifetime of the TAPB-TaBr$_2$ COF and (COF)$_{2.5}$-NH$_2$-M (open circle for data point; solid line for fitting results).

interactions (Supplementary Figs. 20c–f). In Fig. 2g, the polycrystalline domains of TAPB-TaBr$_2$ COF appear widely distributed and interspersed with darker $Ti_3C_2T_x$-NH$_2$ fringes by high-resolution transmission electron microscopy (HR-TEM). Each COF domain displays a honeycomb-like hexagonal framework with a pore size of 3.52 nm, while the MXene lattice fringes exhibit an interplanar spacing of 3.61 nm (Fig. 2h, i). At higher resolution (Supplementary Fig. 21), well-defined boundaries indicate effective supramolecular bridging. Correspondingly, energy-dispersive spectroscopy (EDS) mappings (Supplementary Figs. 22–25) and line scans (Fig. 2j) on different sites corroborate the existence of uniform supramolecular structure arising from hydrogen-bonded connections.

Energy levels and photogenerated carrier dynamics

The electronic structure governs charge carrier dynamics of COFs, which is crucial for evaluating the performance of supramolecular catalysts in practical photosynthesis applications. Theoretical calculations show the highest occupied molecular orbital (HOMO, Fig. 3a) is localized on the donor knots (TAPB), while the lowest unoccupied molecular orbital (LUMO, Fig. 3b) resides on the acceptor linkers (TaBr$_2$), establishing segregated oxidation and reduction sites. To analyze its band structure, the semiconductor energy levels of TAPB-TaBr$_2$ COF and the work function of $Ti_3C_2T_x$-NH$_2$ were separately measured (Fig. 3c). The TAPB-TaBr$_2$ COF yields an optical bandgap of 2.50 eV, as determined from the Tauc plot (Supplementary Fig. 26a).

The conduction band minimum (CBM) of TAPB-$TaBr_2$ COF was determined to be −1.58 V (versus normal hydrogen electrode (NHE), pH 6.8) from the Mott-Schottky plot (Supplementary Fig. 26b), which indicates sufficient driving force for ORR into H_2O_2 via the superoxide anion intermediate ($O_2/^*O_2^-$, − 0.35 V). Meanwhile, its valence band maximum (VBM) lies at 0.92 V (NHE, pH 6.8), suggesting the involvement of $4e^-$ WOR (0.83 V). Ultraviolet photoemission spectroscopy (UPS) (Supplementary Fig. 26c, d) reveals a work function of 3.97 eV for metallic $Ti_3C_2T_x$-NH_2, promoting the formation of Schottky junction with accelerated charge transfer[24]. Based on the band structures predicted by DFT (Fig. 3d, Supplementary Fig. 27, and Supplementary Data 1), the AA-stacked TAPB-$TaBr_2$ COF exhibits the largest bandgap and highest reduction potential to trigger dual H_2O_2 production pathways. According to the projected density of states (PDOS) for TAPB-$TaBr_2$ COF (Fig. 3d), the energy states near the band edge are primarily contributed by *p*-orbital electrons. Specifically, the Br, N, C atoms on the acceptor linkers exhibit greater electron deficiency, as evidenced by their significantly higher *p*-orbital electron density at the conduction band edge (Supplementary Figs. 28 and 29). Moreover, the electrostatic potential calculations reveal that these acceptor linkers carry the most negative average charges which induce photogenerated carrier localization and O_2 adsorption (Fig. 1d).

Next, we investigated the dynamics of photogenerated carriers in $(COF)_x$-NH_2-M. Nyquist plots from electrochemical impedance spectroscopy (EIS) analysis indicate an obvious light response for $(COF)_x$-NH_2-M (Fig. 3e). By further fitting with an equivalent circuit, the charge transfer resistance is determined to reduce due to enhanced charge migration with increasing MXene content, under both dark conditions and 1 sun (standard solar illumination of 100 mW cm^{-2}) irradiation (Supplementary Fig. 30 and Supplementary Table 6). Steady-state photoluminescence (PL) spectra in Fig. 3f show a progressive reduction in emission intensity of $(COF)_x$-NH_2-M's PL around 600 nm to 640 nm, indicative of more efficient exciton dissociation and suppressed electron-hole recombination. Correspondingly, time-resolved fluorescence measurements further corroborate these findings with the average carrier lifetime extending from 0.69 ns to 2.54 ns as MXene loading increases, reflecting enhanced charge extraction by the conductive MXene domains (Fig. 3g, Supplementary Fig. 31, and Supplementary Table 7). Conclusively, integrating metal-like MXene with the COF creates a supramolecular heterostructure with tailored band structures and optimized carrier dynamics, driving dual-route H_2O_2 production.

Photo-to-thermal conversion performance

Among the $(COF)_x$-NH_2-M series samples, obvious color changes of the yellow COF are observed (Supplementary Fig. 32a). Ultraviolet-visible-near-infrared diffuse reflectance spectroscopy (UV-Vis-NIR DRS) was employed to investigate the full-spectrum optical properties of $(COF)_x$-NH_2-M. As shown in Fig. 4a, metallic $Ti_3C_2T_x$-NH_2 nanosheets exhibit a strong absorption bands around 670 nm and 1100 nm due to the LSPR effect[25]. Compared to the TAPB-$TaBr_2$ COF, $(COF)_x$-NH_2-M shows a substantial broadening of absorption across the entire NIR region, which indicates an improved sunlight utilization beyond 250–500 nm. In addition, NIR absorption increases with MXene content in the supramolecular system (Supplementary Figs. 32b–d). Therefore, the MXene units functionalized supramolecular material that we developed provides opportunities for tailoring light response in the NIR region.

A thermal imaging camera and scanning photothermal microscopy (SPThM) were used to evaluate the enhanced photothermal heating capability of $(COF)_x$-NH_2-M at both macroscopic and localized scales (Supplementary Fig. 33a). As illustrated in Fig. 4b and Supplementary Figs. 33b–f, the temperature of a self-supported $Ti_3C_2T_x$-NH_2 film rapidly reached around 72 °C after exposure to simulated 1 sun irradiation. Under identical conditions, the surface temperature of $(COF)_x$-NH_2-M rose from ~38 °C (pure COF) to 57 °C ($x = 2.5$), attributed to the photothermal effect of the $Ti_3C_2T_x$-NH_2 nanosheets. Under such intentionally controlled MXene loading, the elevated temperature remains within a favorable range for H_2O_2 synthesis kinetics[3]. This optimized temperature range, together with the enhanced stability of $Ti_3C_2T_x$-NH_2, effectively suppresses the secondary decomposition (Supplementary Figs. 34 and 35). For localized photo-to-thermal measurements, SPThM equipped with a UV-NIR light source probed illuminated areas on TAPB-$TaBr_2$ COF and $(COF)_{2.5}$-NH_2-M samples. The MXene photothermal units induce a more pronounced temperature rise, which in turn produced proportional changes in the tip voltage due to heat flow from the heated samples to the SPThM tip[26]. By precisely positioning the SPThM tip on the catalyst surface, a higher light-induced temperature increase of 1.8 °C for $(COF)_{2.5}$-NH_2-M nanoparticles were observed versus 1.0 °C for TAPB-$TaBr_2$ COF under the same irradiation conditions, indicating a superior photothermal response (Fig. 4c).

To visualize localized heating effects throughout the supramolecular catalysts, Kelvin probe force microscopy (KPFM) with an integrated light source was employed to map light-induced variations on surface potential[27]. LSPR-induced hot-electron generation on the MXene surface, together with interfacial charge transfer within $(COF)_x$-NH_2-M increases free-electron density and the measured surface potential. As shown in the topography and surface potential maps (Fig. 4d), UV-NIR light illumination on $(COF)_{2.5}$-NH_2-M sample produced a significant increase in surface potential by 51 mV relative to dark conditions, while only marginal change of 12 mV was observed on TAPB-$TaBr_2$ COF sample (Supplementary Fig. 36). Together, the KPFM and SPThM results reveal enhanced localized photo-to-thermal conversion in $(COF)_x$-NH_2-M, which indicates both elevated temperature for accelerated O_2 activation and enhanced charge transfer for driving photocatalytic reaction.

Photocatalytic H_2O_2 production

The photocatalytic activities of $(COF)_x$-NH_2-M were assessed under simulated sunlight in an open batch reactor by monitoring H_2O_2 formation directly from water and air via colorimetry (Supplementary Fig. 37). H_2O_2 production commenced spontaneously upon the addition of $(COF)_x$-NH_2-M dispersion and light irradiation, with no induction period, gas bubbling, pH adjustment, or sacrificial reagents. Under optimized catalyst dosage (Supplementary Fig. 38a) and reaction temperature, $(COF)_{2.5}$-NH_2-M achieved an enhanced H_2O_2 production of 1.77 mmol g^{-1} within 30 min, around 1.81 times that of TAPB-$TaBr_2$ COF (Fig. 4e). Notably, H_2O_2 production rates scaled with MXene content, whereas a pure $Ti_3C_2T_x$-NH_2 suspension yielded negligible 15 μM over 3 h (Supplementary Fig. 39), highlighting the superior performance contributed by our supramolecular design on catalysts. Photocatalytic H_2O_2 yield experiments conducted under irradiation with different wavelength regions revealed a distinct decrease in activity when the NIR and UV components were excluded (Supplementary Fig. 40). This behavior confirms the existence of a synergetic photo- and photothermal-catalytic effect that accelerates the reaction and enhances the overall catalytic efficiency.

Considering the energy band alignment in Fig. 3c, we proceeded to investigate the dual-route pathways with $2e^-$ ORR and $4e^-$ WOR throughout the catalytic process. To probe the role of O_2 in the photocatalytic H_2O_2 production, reactions were performed under different gas atmospheres (Fig. 4f). Continuous Ar/N_2 flow to deoxygenate the dispersion suppressed H_2O_2 formation for both TAPB-$TaBr_2$ COFs and $(COF)_{2.5}$-NH_2-M dispersions, while O_2 flow significantly increased the H_2O_2 yield. Together with the likewise quenched H_2O_2 production with electron scavenger ($AgNO_3$) addition (Supplementary Fig. 38b), a more specific rotating ring-disk electrode (RRDE) measurements in an O_2-saturated phosphate buffer solution (PBS, pH = 7) confirmed the highly selective $2e^-$ ORR pathway for catalytic process (Supplementary

https://doi.org/10.1038/s41467-026-70693-9

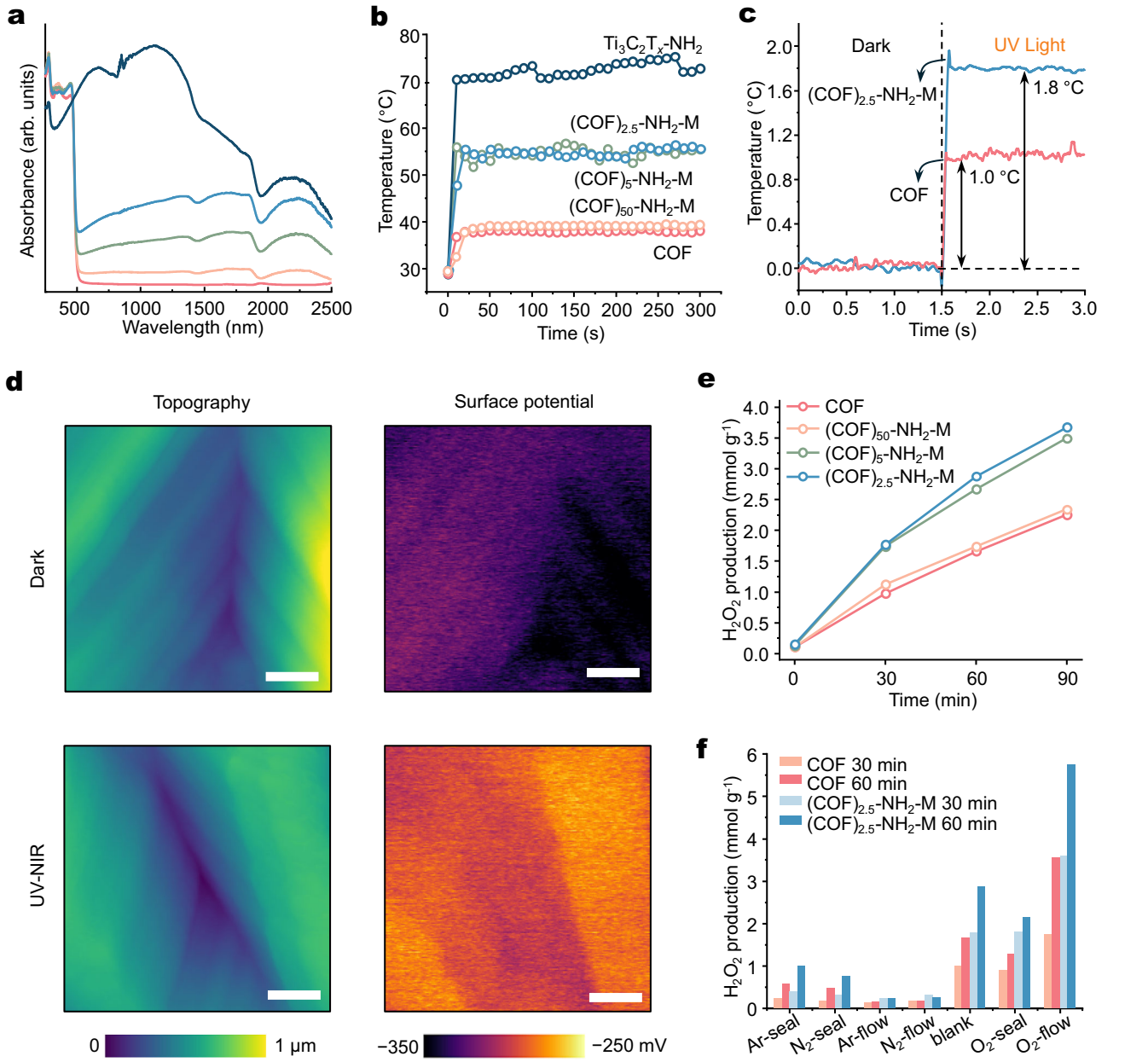

Fig. 4 | Light response and photocatalytic performance of supramolecular (COF)$_x$-NH$_2$-M. a Light absorption spectra of $Ti_3C_2T_x$-NH$_2$ (dark blue),TAPB-TaBr$_2$ COF (red), and (COF)$_x$-NH$_2$-M (orange for $x = 50$; green for $x = 5$; blue for $x = 2.5$) produced by Kubelka-Munk function. **b** Photothermal temperature profiles of thin film samples under 100 mW cm^{-2} light irradiation. **c** Localized temperature variation induced by light-to-heat conversion at a selected spot of (COF)$_{2.5}$-NH$_2$-M. **d** Topography and surface potential maps of a selected area of (COF)$_{2.5}$-NH$_2$-M at dark condition and UV-NIR irradiation (scale bar: 200 nm). **e** H_2O_2 production of TAPB-TaBr$_2$ COF and (COF)$_x$-NH$_2$-M over 90 min. Reaction condition: deionized water (10 mL), catalyst (1 mg), 300 W Xe lamp (full spectrum), peak light intensity: 200 mW cm^{-2}, without aeration or sacrificial agent. **f** H_2O_2 production of TAPB-TaBr$_2$ COF and (COF)$_{2.5}$-NH$_2$-M over 60 min under different gas conditions (seal: reaction solution is purged with relevant gas for 30 min before reaction and then sealed during the reaction; flow: reaction solution is purged with relevant gas for 30 min before reaction and continuously purged throughout the reaction process).

Fig. 41a, b). Noticing the persisted H_2O_2 generation when the reactor was purged with inert gas only before reaction, ORR is expected to sustain owing to the in situ O_2 produced via the 4e$^-$ WOR (oxygen evolution reaction, OER, 0.83 V) which is thermodynamically favored over the 2e$^-$ WOR (1.36 V). Beyond this, the distinct current response for RRDE curves in Ar-saturated PBS (Supplementary Fig. 41c) coincides with the increasing $^{18}O_2/^{16}O_2$ ratios with irradiation time in isotope labeling experiment for sealed photocatalytic system starting with $^{16}O_2$ saturated $H_2{}^{18}O$ solution (Fig. 5a), confirming the existence of 4e$^-$ WOR. Additionally, the $^{18}O_2$ signal remains detectable when the extracted aqueous phase after irradiation was then purged with Ar and injected into a vial containing MnO_2, depicting that the in situ generated O_2 from WOR could subsequently participate in ORR toward H_2O_2.

To verify the possible intermediates involved in photocatalytic production, in situ electron paramagnetic resonance (EPR) spectroscopy was conducted in methanol/H_2O using 5,5-dimethyl-1-pyrroline N-oxide (DMPO) as spin-trapping reagent. As depicted in Fig. 5b, the EPR spectra of both TAPB-TaBr$_2$ COF and (COF)$_{2.5}$-NH$_2$-M dispersion exhibited intensified characteristic peaks of O_2^- with increasing

https://doi.org/10.1038/s41467-026-70693-9

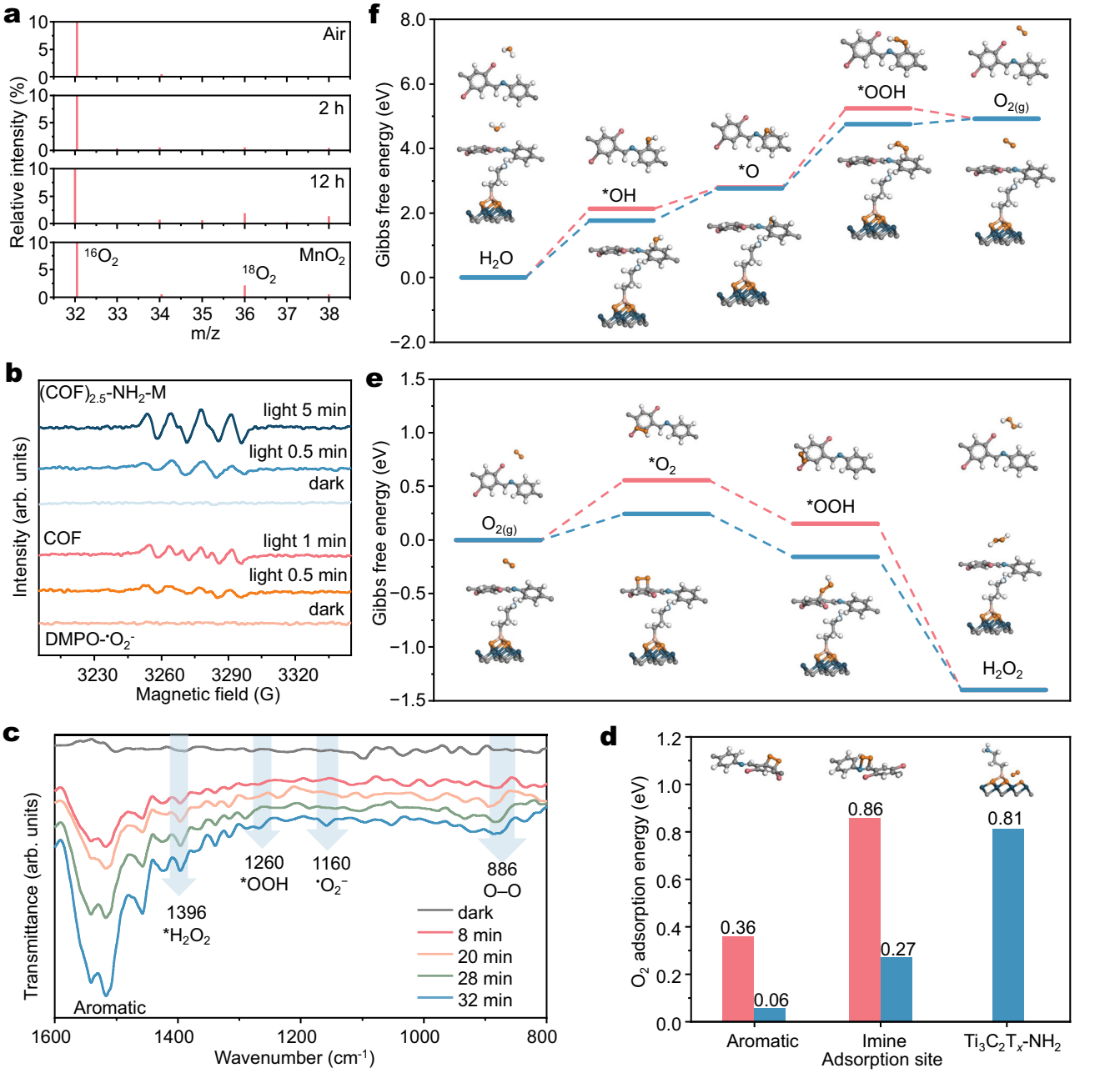

Fig. 5 | In situ analysis and reaction pathways. a $^{18}O_2$ isotope labeling experiment for $(COF)_{2.5}$-NH_2-M system dispersed in $^{16}O_2$ saturated $H_2{}^{18}O$. **b** In situ EPR spectra of TAPB-$TaBr_2$ COF and $(COF)_{2.5}$-NH_2-M reaction solution under dark and light irradiation for different time to capture $^{\bullet}O_2^-$ intermediate with DMPO. **c** In situ DRIFTS spectra of $(COF)_{2.5}$-NH_2-M collected at different photoirradiation time under O_2 and H_2O environment (blue arrows: characteristic peaks of oxygen species). **d** O_2 adsorption energies on aromatic carbon (linker), imine linkage, and oxygen vacancies of MXene (red column, TAPB-$TaBr_2$ COF; blue column, $(COF)_x$-NH_2-M). **e** Gibbs free energy diagram for all intermediates in the oxygen reduction reaction over aromatic carbon (linker) site (red line, TAPB-$TaBr_2$ COF; blue line, $(COF)_x$-NH_2-M). **f** Gibbs free energy diagram for all intermediates in the oxygen evolution reaction over aromatic carbon (knot) site (red line, TAPB-$TaBr_2$ COF; blue line, $(COF)_x$-NH_2-M).

irradiation time, while no signals were detected under dark condition, indicating light-induced generation of O_2^- intermediate. Meanwhile, the more distinct signals in $(COF)_{2.5}$-NH_2-M system suggest accelerated O_2 activation upon light irradiation. In situ diffuse reflectance infrared Fourier transform spectroscopy (DRIFTS) in a sealed chamber with the presence of O_2 and H_2O was employed to further elucidate H_2O_2-formation pathways and identify reactive sites on $(COF)_x$-NH_2-M (Fig. 5c). A broad peak at 886 cm^{-1} corresponding to O–O bonding[13,28,29] gradually increases with irradiation time, suggesting the accumulation of H_2O_2. Moreover, the concurrent emergence and intensification of the OOH bending mode of surface-adsorbed H_2O_2 (*H_2O_2) at 1396 cm^{-1} further reveal in situ H_2O_2 generation[30,31]. Peaks at 1160 cm^{-1} and 1260 cm^{-1} assigned to $^{\bullet}O_2^-$ [28,32] and *OOH[30,31,33,34], respectively, further support the formation of key intermediates in a two-step ORR pathway (Supplementary Fig. 27e). Compared to DRIFTS without O_2 flow (Supplementary Fig. 42a), enhanced aromatic signals between 1400–1600 cm^{-1} indicate that the aromatic rings serve as O_2 docking site. Notably, in situ Raman spectra corroborate the occurrence of $^{\bullet}O_2^-$, evidenced by the signal magnification at 1091 cm^{-1} over time[35] (Supplementary Fig. 42b).

To elucidate the docking mechanism underlying the enhanced H_2O_2 photosynthesis, we combined DFT analysis with spectroscopic

observations and temperature-programmed measurements on TAPB-$TaBr_2$ COF and $(COF)_x$-NH_2-M assemblies. The DRIFTS results show time-dependent variations in the peak intensities of aromatic carbon moieties under photoirradiation, suggesting their likely involvement as active sites (Fig. 5c). Based on this observation and the LUMO distribution of TAPB-$TaBr_2$ COF (Fig. 3b), the imine linkages and adjacent aromatic carbons are selected as candidate O_2 adsorption sites for comparative analysis (Supplementary Figs. 43–45). O_2 adsorption energy calculations on TAPB-$TaBr_2$ COF (Fig. 5d, red columns) indicate that O_2 docking at aromatic carbons (0.36 eV) is energetically more favorable than at imine linkages (0.86 eV). The incorporation of $Ti_3C_2T_x$-NH_2 units in $(COF)_x$-NH_2-M contributes to the electron abundance on COF framework with lower O_2 adsorption energy at aromatic carbons (0.06 eV), suggesting the facilitated O_2 docking at COF framework (Fig. 5d, blue columns). In comparison, oxygen vacancies of $Ti_3C_2T_x$-NH_2 exhibit a high adsorption energy (0.81 eV), implying limited likelihood of effective O_2 activation at these sites. To experimentally evaluate the O_2 docking capability of materials, oxygen temperature-programmed desorption (O_2-TPD) was performed to probe the adsorption-desorption behavior of surface oxygen species. Prior to the O_2-TPD measurements, thermogravimetric analysis verified the thermal stability of the TAPB-$TaBr_2$ COF over the relevant temperature range (Supplementary Fig. 46). The TPD profiles exhibit a pronounced low-temperature desorption feature (~150 °C), which can be attributed to reversible oxygen species that are weakly bound at π-conjugated aromatic carbon sites[36] (Supplementary Fig. 47). Notably, the increasing MXene content leads to a pronounced enhancement of the low-temperature desorption, indicating the improved O_2 docking capability in $(COF)_x$-NH_2-M. Furthermore, Gibbs free energy calculations disclose a lower energy barrier toward forming the $*O_2$ intermediate at the aromatic carbon site of $(COF)_x$-NH_2-M (Fig. 5e), which is the rate-determining step of ORRs. Similarly, OER is expected to proceed via a single-site (*O/*OOH) pathway at the aromatic carbons located at the TAPB edge, where $(COF)_x$-NH_2-M exhibits a lower energy barrier (1.993 eV) than TAPB-$TaBr_2$ COF (2.492 eV) (Fig. 5f). It should be noted that the calculated free-energy profiles serve as thermodynamic descriptors of elementary steps and do not directly represent absolute photocatalytic reaction kinetics. Nevertheless, the consistency between the computed energetic trends and the experimentally established reaction pathways, together with the enhanced catalytic performance of the supramolecular systems, provides qualitative support to the proposed ORR/WOR mechanism and more favorable reaction energetics upon MXene incorporation.

Practical potential assessment

To investigate the stability of $(COF)_{2.5}$-NH_2-M, a recycling test was performed, presenting a negligible H_2O_2 yield decay and minor structural changes within 5 cycles (Supplementary Fig. 48). To evaluate the scalability and real-world applicability of our photocatalytic system, we designed an integrated flow reactor incorporating $(COF)_x$-NH_2-M dispersions. Coupled with a peristaltic pump and a collection reservoir, the aqueous $(COF)_{2.5}$-NH_2-M dispersion was continuously circulated through modular tandem reactors. This setup enabled uninterrupted H_2O_2 generation over 24 h under laboratory conditions without noticeable activity loss (Supplementary Fig. 49), which can be attributed to the robust π-conjugated framework of $(COF)_x$-NH_2-M supramolecular assembly. To further validate practical viability, we deployed a self-powered outdoor system driven by a photovoltaic cell (Fig. 6a), which sustained a steady production of H_2O_2 at a peak rate of 658 μmol g^{-1} h^{-1} under ambient conditions (light intensity <1 sun) as shown in Supplementary Fig. 50.

Importantly, in many decentralized applications, such as environmental disinfection, food preservation, and green chemistry, the required H_2O_2 concentration at the point of use is typically below 0.4 wt%[37]. This stands in stark contrast to conventional AO processes, which generate highly concentrated H_2O_2 solution that requires subsequent distillation and poses substantial safety risks during transport and storage. To address this, we proposed a modular collection platform (Fig. 6b) to directly produce controllable concentrations of H_2O_2 on-site, thus eliminating the demands for energy-intensive post-processing and mitigating explosion hazards. In addition, immobilizing $(COF)_{2.5}$-NH_2-M supramolecular catalyst on a solid substrate facilitated continuous replenishment of the reaction medium and prolonged the operational lifespan while maintaining consistent productivity. As a result, the total amount of H_2O_2 accumulated linearly over time (Supplementary Figs. 51 and 52). Among state-of-the-art photocatalytic H_2O_2 production system[11,13,17,29,34,38–46], our system delivers a competitive production rate of 2,878 μmol g^{-1} h^{-1} without requiring O_2 bubbling, pH adjustment, or sacrificial agent. Notably, this is the first demonstration of continuous operation for 1,008 h in a fully integrated setup (Fig. 6c and Supplementary Table 8). This combination of operational simplicity, long-term durability, and point-of-use compatibility offers a promising pathway for advancing photocatalytic H_2O_2 production toward real-world applications.

We also evaluated the photocatalytic performance of $(COF)_{2.5}$-NH_2-M in deionized water, simulated seawater, and real seawater. Only a slight decrease in H_2O_2 production was observed (Fig. 6d), suggesting that the material retains high activity despite potential interference from competing ions. To further demonstrate practical applicability, we conducted in situ pollutant removal tests using methyl orange (MO) and 2,4,6-triformylphloroglucinol (TFP) as representative dye and phenolic pollutants (Supplementary Fig. 53). Under 1 sun irradiation, rapid degradation of MO (95%) and TFP (77%) was achieved within 60 min (Fig. 6e), confirming not only the reactivity of the produced H_2O_2 but also the system's broad potential for decentralized water treatment scenarios. The on-demand generation of dilute H_2O_2 solutions minimizes the need for transporting, storing, and handling concentrated oxidants, thereby offering an inherently safer and more sustainable disinfection route. As evidenced by the global solar irradiance map (Supplementary Fig. 54), the widespread distribution of solar resources supports the feasibility of deploying $(COF)_x$-NH_2-M-integrated systems across diverse regions. Operating under ambient conditions without external energy input or hazardous reagents, this platform offers an environmentally benign, decentralized, and scalable alternative to the conventional AO H_2O_2 industry.

Discussion

Our work proposes a metallic unit-functionalized supramolecular docking strategy for targeted reactant adsorption to overcome long-standing challenges in the intrinsic activity and catalytic selectivity of COFs. By engineering precise σ–π stacking interactions in $(COF)_x$-NH_2-M, we not only synergistically enhance of charge carrier dynamics and light absorption but also facilitates site-specific capture of O_2 and H_2O, enabling H_2O_2 production under ambient conditions without external gas feeds, pH-regulation, or sacrificial agents. The demonstrated activity of 2878 μmol g^{-1} h^{-1} in batch reactors and over 1008 h of stable production in continuous flow highlights robustness and scalability of the system. The generated H_2O_2 can be utilized in situ for efficient pollutant removal, without limitations from the water source. Beyond these benchmarks, our supramolecular docking strategy provides a modular and generalizable platform for designing next-generation COF-based catalysts with programmable structure–function relationships. By integrating reactant capture, chemical conversion, and product utilization "capture-synthesis-utilization" into a single system, this approach unlocks precision-driven and distributed chemical manufacturing.

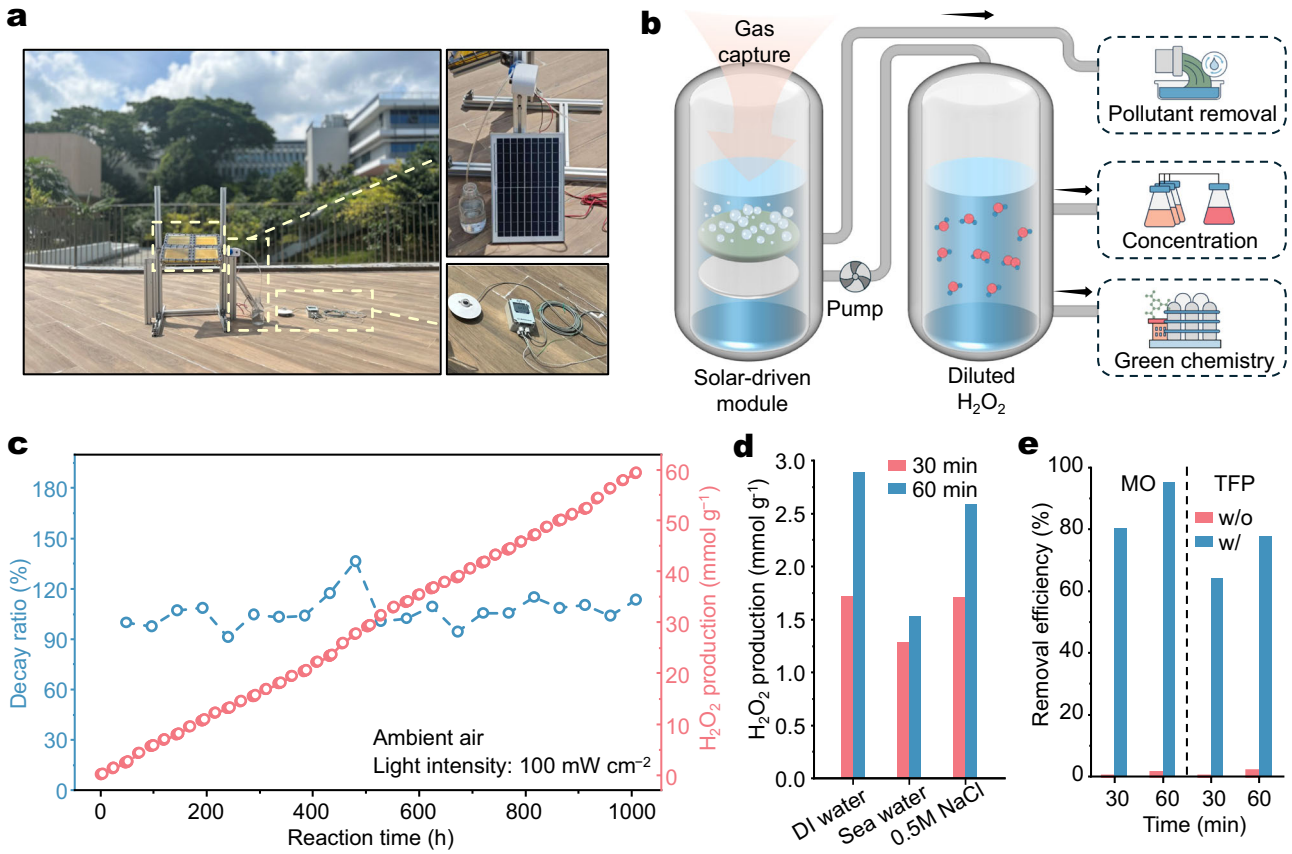

Fig. 6 | Practical application and performance of $(COF)_x$-NH_2-M. a Digital photograph of scale-up reactor under ambient environment. **b** A schematic demonstration of an integrated industrial system for capture-synthesis-utilization. **c** Catalytic stability of flow-system with operation over 1000 h. Test condition: deionized water (0.5 mL min^{-1}), catalyst (15 mg), 300 W Xe lamp (full spectrum), peak light intensity: 100 mW cm^{-2}, without sacrificial agent. **d** H_2O_2 production of TAPB-$TaBr_2$ COF (red) and $(COF)_{2.5}$-NH_2-M (blue) over 60 min using different water source. **e** Removal efficiencies of MO and TFP pollutants by $(COF)_{2.5}$-NH_2-M over 60 min (w/o: without catalyst; w/: with catalyst).

Methods

Materials

TAPB, $TaBr_2$, mesitylene, 1,4-dioxane, acetic acid, ethanol, acetone, lithium fluoride, hydrochloric acid (HCl, 37%), APTES, potassium hydrogen phthalate (KHP), potassium iodide (KI), and Nafion (5 wt% in the mixture of lower aliphatic alcohols and water) were purchased from Adamas. D_2O (≥99.9 at% D), Water-^{18}O (≥97 at% ^{18}O), and DMPO (≥97%) were purchased from Aladdin. Titanium aluminum carbide (Ti_3AlC_2, MAX) was purchased from Laizhou Kai Kai Ceramic Materials Co. Ltd. All chemicals were used as received without further purification.

Synthesis of TAPB-$TaBr_2$ COF

To synthesize TAPB-$TaBr_2$ COFs, 0.4 mmol TAPB (140.58 mg) and 0.6 mmol $TaBr_2$ (175.15 mg) were added into a Teflon reactor and ultrasonically dispersed for 20 min in 10 mL mixed solvent of mesitylene/1,4-dioxane (v: v = 1:4). Subsequently, 1 mL acetic acid solution (6 M) was added and followed by another 5 min ultrasonication. The reactor was then sealed and transferred to an oven at 120 °C. After 3 days of solvothermal reaction, the precipitate was washed three times with acetone and ethanol respectively and collected by suck filtration through hydrophobic membranes. Finally, the product was ground with ethanol and dried in vacuum oven at 60 °C for 12 h.

Synthesis of $Ti_3C_2T_x$-NH_2

The $Ti_3C_2T_x$ suspension (30 mg in 3 mL ethanol and 12 mL H_2O), obtained by wet etching of HCl/LiF and ethanol addition, was stirred with 1 mL APTES for 12 h at ambient temperature. After centrifuging sequentially in ethanol and H_2O, the precipitate was freeze-dried for 2 days to obtain $Ti_3C_2T_x$-NH_2.

Synthesis of $(COF)_x$-NH_2-M

To synthesize $(COF)_x$-NH_2-M, $Ti_3C_2T_x$-NH_2 powder was finely ground and then sonicated to disperse in the mixture of 0.4 mmol TAPB (140.58 mg), 0.6 mmol $TaBr_2$ (175.15 mg), and 10 mL mixed solvent of mesitylene/1,4-dioxane (v: v = 1:4), where the $Ti_3C_2T_x$-NH_2 content was determined by the mass ratio to the feeding amount of COF monomers (x). After the addition of 1 mL acetic acid solution (6 M), the following sonication time was prolonged to 20 min to further ensure thorough mixing of the COF monomers and $Ti_3C_2T_x$-NH_2 nanosheets. Finally, the product after subsequent solvothermal reaction and collection were conducted inductively coupled plasma optical emission spectroscopy (ICP-OES) and CHNS measurements for elemental analysis to verify the repeatability.

Photocatalytic H_2O_2 synthesis and quantification

For batch reactor, 1 mg of photocatalyst was dispersed in 10 mL deionized water. A 300 W Xe lamp (CEL-PE300-3A, China Education Au-light) was calibrated with a light intensity meter and used to drive the photocatalytic reaction with magnetic stirring at 150 rpm. The reaction solution was sampled at certain intervals and passed through hydrophilic syringe filters. The yield of H_2O_2 was determined by iodometry method (0.5 mL reaction solution + 0.5 mL deionized water + 1 mL 0.1 M KHP + 1 mL 0.4 M KI) and followed by UV-Vis spectroscopy

to determine the concentration of I_3^- oxidized by H_2O_2. For flow reactor, 15 mg photocatalyst was dispersed in the mixture of 4.5 mL ethanol and 0.5 mL Nafion (binder), subsequently deposited on the substrate. Deionized water was continuously pumped into the reactor and the diluted H_2O_2 solution was collected in the source container. A controlled amount of catalyst was periodically replenished to offset stripping.

Materials characterization

The valence state and work function of as-prepared samples were measured by XPS (Al Kα source) and UPS (ESCALAB 250Xi, Thermo Fisher Scientific). The PXRD patterns were recorded on a diffractometer (D8 Advance, Bruker, Cu Kα radiation), together with BET test (3Flex, Micromeritics) to further analyze the crystal structure and mesoporosity. The chemical bonding was determined by Raman spectroscopy (WITec alpha300, Oxford Instruments) and FTIR (IRPrestige-21, Shimadzu). The morphology was revealed by SEM (JSM-7001F, JEOL) and HRTEM (JEM-F200, JEOL). Steady-state PL spectra and time-resolved fluorescence lifetime were recorded by spectrofluorometer (FLS1000, Edinburgh) under 364 nm excitation light. The reflectance and absorbance spectra were obtained using an UV-Vis-NIR spectrophotometer (UV-3600, Shimadzu). The chemical adsorption characteristics were evaluated by thermogravimetric analysis (STA200, HITACHI) and O_2-TPD (TP-5080B, Xianquan).

Independent gradient model based on Hirshfeld partition (IGMH)

The DFT calculations on molecular cluster model was performed using the Gaussian 16 package[47]. Geometry optimizations and vibrational frequency calculations were carried out with the BL3YP-D3[48–50], employing the lanl2dz basis set for Br atom and the 6-31 G (d)[51] basis set for other elements. Using optimized structure, the IGMH[52] was employed to analyze with Multiwfn[53] and visualize with Visual Molecular Dynamics[54] software.

Nuclear magnetic resonance (NMR) measurements

The solution-state ^{1}H NMR (Varian mercury 400, Agilent, D_2O as solvent) was applied to analyze the successful grafting of $-NH_2$ groups on $Ti_3C_2T_x$. The solid-state ^{1}H and ^{13}C CP/MAS NMR (Avance Neo 400 M, Bruker) were performed to validate the existence of N−H···N hydrogen bonding interactions, which were further verified by the variable-temperature ^{1}H solid-state NMR (Avance Neo 400WB, Bruker) measurements at MAS = 15 kHz.

Electrochemical measurements

The electrochemical impedance spectroscopy (EIS) and Mott-Schottky measurements were conducted using a CHI660E electrochemical workstation configured in a standard three-electrode system. The working electrode was prepared by coating the catalyst on fluorine-doped tin oxide substrates, while a platinum plate and an Ag/AgCl electrode served as the counter and reference electrodes, respectively. All measurements were carried out in the 0.2 M $NaSO_4$ solution[13] (pH = 6.8). EIS was analyzed with a frequency ranging from 100 kHz to 0.1 Hz. The position of conduction band minimum (CBM) can be converted into normal hydrogen electrode (NHE) using the following equation:

$$E_{NHE\,(pH=6.8)} = E_{AgCl/Ag} + 0.197\ V \tag{1}$$

Scanning photothermal microscopy (SPThM) and Kelvin probe force microscopy (KPFM)

SPThM and KPFM were carried out on a commercial scanning probe microscopy system (MFP-3D, Asylum Research, Oxford Instruments). During the measurements, the samples were irradiated with a metal halide fiber optic illuminator (Model MH-100), covering a full UV-NIR spectrum.

$^{18}O_2$ isotope labeling experiments

The $^{18}O_2$ isotope was measured on a gas chromatograph mass spectrometer (GC-MS, GCMS-QP2010Ultra, Shimadzu). $(COF)_{2.5}$-NH_2-M photocatalyst (2 mg) and $H_2{}^{18}O$ (≥ 97 atom% ^{18}O, 1 mL) were added into a sealed quartz tube and pumped with $^{16}O_2$ in the dark for 30 min. After 2 h and 12 h irradiation, the 60 μL of gas products in the headspace were extracted and analyzed by GC-MS. The remaining liquid phase of mixture was pumped with Ar for 30 min to remove the remaining O_2 and subsequently added with MnO_2 to generate O_2 by the decomposition of photogenerated H_2O_2.

Rotating ring-disk electrode (RRDE) measurements

The ORR and WOR were studied by using a RRDE with $(COF)_{2.5}$-NH_2-M, which was coated using a uniformly dispersed mixture (5 mg photocatalyst in 20 μL 5% Nafion and 180 μL isopropanol). The RRDE assembly included a glassy carbon disk (r = 4 mm) and a platinum ring (r = 4.3 mm/6.3 mm). For ORR, 0.1 M PBS (pH = 7) saturated with O_2 was used as electrolyte, with platinum plate as counter electrode and Ag/AgCl electrode as reference electrode. The ring/disk currents were measured by an SP-150e potentiostat (Biologic). The H_2O_2 product was detected at the ring potential of 0.6 V (vs. Ag/AgCl). The electron transfer number (n) is calculated as follows:

$$n = \frac{4I_d}{I_d + \frac{I_r}{N}} \tag{2}$$

where I_d is the disk electrode current, I_r is the ring electrode current, and N is the collection efficiency.

Similarly, the WOR was analyzed in Ar saturated solution and detected at the ring potential of −0.23 V (vs. Ag/AgCl).

Electron paramagnetic resonance (EPR) spectroscopy

The catalysts (2 mg) were separately dispersed into a methanol/H_2O mixture (9/1 v/v, 500 μL) containing 0.1 mmol DMPO as a spin-trapping reagent to detect $^{\bullet}O_2^-$ intermediate. Before reaction, the dispersion was purged with O_2 gas for 5 min. The resulting mixture was extracted and sealed in a capillary tube, followed by Xe lamp irradiation for subsequent testing.

In situ diffuse reflectance infrared Fourier transform spectroscopy (DRIFTS)

In situ DRIFTS measurements were conducted in an in situ reaction cell (Hefei in situ technology) and detected by a modified FTIR spectrometer (Nicolet iS50, Thermo Fisher Scientific) equipped with an MCT detector cooled by liquid N_2. Before the measurement, the photocatalyst with a small amount of water was filled into the holder and the chamber was purged with He/O_2 gas mixture at a flow rate of 10 mL min^{-1} for 30 min to record the baseline. Subsequently, the Xe lamp was used to irradiate the reaction cell and the IR spectra were collected with time.

Computational details

The simulation of periodic COF structure was conducted on the BIOVIA Materials Studio suite of programs to perform molecular dynamics and DFT calculations within the generalized gradient approximation (GGA)[55] using the Perdew-Burke-Ernzerhof (PBE) functional. The geometry structure was initially established in the Forcite module and followed by optimization in the $DMoL^3$ module. During the structural optimization, we employed an energy convergency smaller than 2×10^{-5} Ha. Pawley refinement was then predicted using Reflex module with convergent R_{wp} and R_p. For energy calculation, we used the k-point set of 1 × 1 × 4 to sample the electronic structure.

To simulate the H_2O_2 generation, we employed the Vienna Ab initio Simulation Package (VASP)[56,57] at GGA-PBE level with *k*-points of $1 \times 1 \times 1$. The interaction between valence electrons and ionic cores was treated with the projected augmented wave method[58] with an energy cutoff of 450 eV. To account for long-range dispersion interactions, the DFT-D3 empirical correction was incorporated[59].

More discussions of the DFT calculation are listed in the supplementary information.

Data availability

All data that support the findings of this study are available within the article and Supplementary Information. Source data are provided with this paper.

References

1. Ciriminna, R., Albanese, L., Meneguzzo, F. & Pagliaro, M. Hydrogen peroxide: a key chemical for today's sustainable development. *ChemSusChem* **9**, 3374–3381 (2016).
2. Sanlı, A. E. A possible future fuel cell: the peroxide/peroxide fuel cell. *Int. J. Energy Res.* **37**, 1488–1497 (2013).
3. Campos-Martin, J. M., Blanco-Brieva, G. & Fierro, J. L. G. Hydrogen peroxide synthesis: an outlook beyond the anthraquinone process. *Angew. Chem. Int. Ed.* **45**, 6962–6984 (2006).
4. Jung, E. et al. Atomic-level tuning of Co–N–C catalyst for high-performance electrochemical H_2O_2 production. *Nat. Mater.* **19**, 436–442 (2020).
5. Hou, H., Zeng, X. & Zhang, X. Production of hydrogen peroxide by photocatalytic processes. *Angew. Chem. Int. Ed.* **59**, 17356–17376 (2020).
6. Li, B. et al. Photocatalysis driven by near-infrared light: materials design and engineering for environmentally friendly photoreactions. *ACS EST Eng.* **1**, 947–964 (2021).
7. Feng, A. et al. σ–σ Stacked supramolecular junctions. *Nat. Chem.* **14**, 1158–1164 (2022).
8. Ascherl, L. et al. Molecular docking sites designed for the generation of highly crystalline covalent organic frameworks. *Nat. Chem.* **8**, 310–316 (2016).
9. Tan, K. T. et al. Covalent organic frameworks. *Nat. Rev. Methods Prim.* **3**, 1–19 (2023).
10. Mullangi, D. et al. Noncryogenic air separation using aluminum formate $Al(HCOO)_3$ (ALF). *J. Am. Chem. Soc.* **145**, 9850–9856 (2023).
11. Qin, C. et al. Dual donor-acceptor covalent organic frameworks for hydrogen peroxide photosynthesis. *Nat. Commun.* **14**, 5238 (2023).
12. Chi, W., Wu, J., Dong, Y., Wu, J. & Zhu, Y. Accelerated exciton dissociation and charge transfer via third-motif engineered conjugated polymers for photocatalytic circulation-flow synthesis of H_2O_2. *Angewandte Chemie Int. Ed.* **64**, e202508690 (2025).
13. Liu, R. et al. Linkage-engineered donor–acceptor covalent organic frameworks for optimal photosynthesis of hydrogen peroxide from water and air. *Nat. Catal.* **7**, 195–206 (2024).
14. Lyu, J. et al. Ultra-large library docking for discovering new chemotypes. *Nature* **566**, 224–229 (2019).
15. Bender, B. J. et al. A practical guide to large-scale docking. *Nat. Protoc.* **16**, 4799–4832 (2021).
16. Wu, Y. et al. Supramolecular docking structure determination of alkyl-bearing molecules. *Nature* **640**, 676–682 (2025).
17. Zhao, W. et al. Accelerated synthesis and discovery of covalent organic framework photocatalysts for hydrogen peroxide production. *J. Am. Chem. Soc.* **144**, 9902–9909 (2022).
18. Zhu, D. et al. Understanding fragility and engineering activation stability in two-dimensional covalent organic frameworks. *Chem. Sci.* **13**, 9655–9667 (2022).
19. Ji, J., Zhao, L., Shen, Y., Liu, S. & Zhang, Y. Covalent stabilization and functionalization of MXene via silylation reactions with improved surface properties. *FlatChem* **17**, 100128 (2019).
20. Tian, J. et al. Hydrogen-bonded supramolecular polymer networks for effective removal of perchlorate in water via clustered hydrogen-bonding. *Nat. Commun.* **16**, 6481 (2025).
21. Liu, M. et al. Two-dimensional covalent organic framework films prepared on various substrates through vapor induced conversion. *Nat. Commun.* **13**, 1411 (2022).
22. Guerin, A. C., Riley, K., Rupnik, K. & Kuroda, D. G. Determining the energetics of the hydrogen bond through FTIR: a hands-on physical chemistry lab experiment. *J. Chem. Educ.* **93**, 1124–1129 (2016).
23. Leng, K. et al. Hydrogen-bonded dimer dissociation under MOF nanoconfinement enables thermal transition tailoring of medium-chain fatty acids. *J. Am. Chem. Soc.* **147**, 39623–39631 (2025).
24. Li, J. et al. Interfacial engineering of $Bi_2S_3/Ti_3C_2T_x$ MXene based on work function for rapid photo-excited bacteria-killing. *Nat. Commun.* **12**, 1–10 (2021).
25. Lin, H., Wang, X., Yu, L., Chen, Y. & Shi, J. Two-dimensional ultrathin MXene ceramic nanosheets for photothermal conversion. *Nano Lett.* **17**, 384–391 (2017).
26. Wu, L. et al. Photothermal-promoted anion exchange membrane seawater electrolysis on a nickel-molybdenum-based catalyst. *Nat. Commun.* **16**, 3098 (2025).
27. Ng, S. W. L., Gao, M., Lu, W., Hong, M. & Ho, G. W. Selective wavelength enhanced photochemical and photothermal H_2 generation of classical oxide supported metal catalyst. *Adv. Funct. Mater.* **31**, 2104750 (2021).
28. Liao, Q. et al. Regulating relative nitrogen locations of diazine functionalized covalent organic frameworks for overall H_2O_2 photosynthesis. *Angew. Chem. Int. Ed.* **62**, e202310556 (2023).
29. Liu, F. et al. Covalent organic frameworks for direct photosynthesis of hydrogen peroxide from water, air and sunlight. *Nat. Commun.* **14**, 4344 (2023).
30. Sun, L., Jin, X., Su, T., Fisher, A. C. & Wang, X. Conjugated nickel phthalocyanine derivatives for heterogeneous electrocatalytic H_2O_2 synthesis. *Adv. Mater.* **36**, 2306336 (2024).
31. Li, Y. et al. Single-atom iron catalyst with biomimetic active center to accelerate proton spillover for medical-level electrosynthesis of H_2O_2 disinfectant. *Angew. Chem. Int. Ed.* **62**, e202306491 (2023).
32. Kou, M. et al. Molecularly engineered covalent organic frameworks for hydrogen peroxide photosynthesis. *Angew. Chem. Int. Ed.* **61**, e202200413 (2022).
33. Cao, P. et al. Metal single-site catalyst design for electrocatalytic production of hydrogen peroxide at industrial-relevant currents. *Nat. Commun.* **14**, 172 (2023).
34. Liu, Y. et al. Enhanced hydrogen peroxide photosynthesis in covalent organic frameworks through induced asymmetric electron distribution. *Nat. Synth.* **4**, 134–141 (2025).
35. Dong, J.-C. et al. In situ Raman spectroscopic evidence for oxygen reduction reaction intermediates at platinum single-crystal surfaces. *Nat. Energy* **4**, 60–67 (2019).
36. Guo, Y. et al. Enhanced hydrogen peroxide photosynthesis via charge-complementary π-electron sites. *Nat. Commun.* **16**, 6297 (2025).
37. Li, S., Ma, J., Xu, F., Wei, L. & He, D. Fundamental principles and environmental applications of electrochemical hydrogen peroxide production: A review. *Chem. Eng. J.* **452**, 139371 (2023).
38. Chen, D. et al. Covalent organic frameworks containing dual O_2 reduction centers for overall photosynthetic hydrogen peroxide production. *Angew. Chem. Int. Ed.* **62**, e202217479 (2023).
39. Liu, Y. et al. Fluorination of covalent organic framework reinforcing the confinement of Pd nanoclusters enhances hydrogen peroxide photosynthesis. *J. Am. Chem. Soc.* **145**, 19877–19884 (2023).

40. Chakraborty, A. et al. Enhancing photocatalytic hydrogen peroxide generation by tuning hydrazone linkage density in covalent organic frameworks. *Nat. Commun.* **16**, 503 (2025).
41. Hou, Y. et al. Efficient photosynthesis of hydrogen peroxide by cyano-containing covalent organic frameworks from water, air and sunlight. *Angew. Chem.* **136**, e202318562 (2024).
42. Rodríguez-Camargo, A. et al. Cyclopalladation of a covalent organic framework for near-infrared-light-driven photocatalytic hydrogen peroxide production. *Nat. Synth.* **4**, 710–719 (2025).
43. Shu, C. et al. Mixed-linker strategy for the construction of sulfone-containing D–A–A covalent organic frameworks for efficient photocatalytic hydrogen peroxide production. *Angew. Chem. Int. Ed.* **63**, e202403926 (2024).
44. Zhang, Y. et al. H_2O_2 generation from O_2 and H_2O on a near-infrared absorbing porphyrin supramolecular photocatalyst. *Nat. Energy* **8**, 361–371 (2023).
45. Kofuji, Y. et al. Carbon nitride–aromatic diimide–graphene nanohybrids: metal-free photocatalysts for solar-to-hydrogen peroxide energy conversion with 0.2% efficiency. *J. Am. Chem. Soc.* **138**, 10019–10025 (2016).
46. Tan, H. et al. Photocatalysis of water into hydrogen peroxide over an atomic Ga-N_5 site. *Nat. Synth.* **2**, 557–563 (2023).
47. Frisch, M. J. et al. Gaussian 16, Revision A.03. (2016).
48. Becke, A. D. Density-functional thermochemistry. III. *Role Exact. Exch. J. Chem. Phys.* **98**, 5648–5652 (1993).
49. Lee, C., Yang, W. & Parr, R. G. Development of the Colle-Salvetti correlation-energy formula into a functional of the electron density. *Phys. Rev. B* **37**, 785–789 (1988).
50. Grimme, S., Antony, J., Ehrlich, S. & Krieg, H. A consistent and accurate ab initio parametrization of density functional dispersion correction (DFT-D) for the 94 elements H-Pu. *J. Chem. Phys.* **132**, 154104 (2010).
51. Francl, M. M. et al. Self-consistent molecular orbital methods. XXIII. A polarization-type basis set for second-row elements. *J. Chem. Phys.* **77**, 3654–3665 (1982).
52. Lu, T. & Chen, Q. Independent gradient model based on Hirshfeld partition: a new method for visual study of interactions in chemical systems. *J. Comput.Chem.* **43**, 539–555 (2022).
53. Lu, T. & Chen, F. MultiWFN: a multifunctional wavefunction analyzer. *J. Comput. Chem.* **33**, 580–592 (2012).
54. Humphrey, W., Dalke, A. & Schulten, K. VMD: visual molecular dynamics. *J. Mol. Graph.* **14**, 33–38 (1996).
55. Perdew, J. P., Burke, K. & Ernzerhof, M. Generalized gradient approximation made simple. *Phys. Rev. Lett.* **77**, 3865–3868 (1996).
56. Kresse, G. & Furthmüller, J. Efficiency of ab-initio total energy calculations for metals and semiconductors using a plane-wave basis set. *Comput. Mater. Sci.* **6**, 15–50 (1996).
57. Kresse, G. & Hafner, J. Ab initio molecular-dynamics simulation of the liquid-metal-amorphous-semiconductor transition in germanium. *Phys. Rev. B* **49**, 14251–14269 (1994).
58. Kresse, G. & Joubert, D. From ultrasoft pseudopotentials to the projector augmented-wave method. *Phys. Rev. B* **59**, 1758–1775 (1999).
59. Tang, S. et al. 3D-orbital overlap modulated d-band center of high-entropy oxyhydroxide for efficient oxygen evolution reaction. *Appl. Surf. Sci.* **682**, 161760 (2025).

Acknowledgements

This research is supported by the Ministry of Education, Singapore, under the Academic Research Fund Tier 1 (FY2023, A-8002151-00-00, G.W.H), and NUS research support (A-8003994-00-00, G.W.H).

Author contributions

G.W.H. and Y.M.Z. guided the project. J.X.S. and Y.M.Z. conceived the research and designed the experiments. J.X.S. prepared the materials and carried out the experiments. W.H.L. performed the AFM and KPFM experiments. J.X.S., Y.M.Z., and W.L.O. contributed to the batch reactor and flow reactor design. X.L.P. contributed to the FTIR and Raman measurements. J.X.S., Y.M.Z., and X.L.P. performed the materials studio calculations. W.T.S. conducted the photoluminescence tests. Y.M.Z., Z.H.L., and Z.S.L. performed the in situ DRIFTS test. J.X.S., Y.M.Z., and G.W.H. wrote the paper. All authors read and commented on the paper.

Competing interests

The authors declare no competing interests.

Additional information

Supplementary information The online version contains supplementary material available at https://doi.org/10.1038/s41467-026-70693-9.

Correspondence and requests for materials should be addressed to Ghim Wei Ho.

Peer review information *Nature Communications* thanks the anonymous, reviewer(s) for their contribution to the peer review of this work. A peer review file is available.